



**HAL**  
open science

## Origin of $112 < 111 >$ antitwinning in a Ti-24Nb-4Zr-8Sn superelastic single crystal

Emmanuel Bertrand, Philippe Castany, Yang Yang, Edern Menou, Laurent  
Couturier, Thierry Gloriant

### ► To cite this version:

Emmanuel Bertrand, Philippe Castany, Yang Yang, Edern Menou, Laurent Couturier, et al.. Origin of  $112 < 111 >$  antitwinning in a Ti-24Nb-4Zr-8Sn superelastic single crystal. *Journal of Materials Science*, 2022, 57 (14), pp.7327-7342. 10.1007/s10853-022-07086-y . hal-03657815

**HAL Id: hal-03657815**

**<https://hal.science/hal-03657815>**

Submitted on 20 May 2022

**HAL** is a multi-disciplinary open access archive for the deposit and dissemination of scientific research documents, whether they are published or not. The documents may come from teaching and research institutions in France or abroad, or from public or private research centers.

L'archive ouverte pluridisciplinaire **HAL**, est destinée au dépôt et à la diffusion de documents scientifiques de niveau recherche, publiés ou non, émanant des établissements d'enseignement et de recherche français ou étrangers, des laboratoires publics ou privés.



Distributed under a Creative Commons Attribution - NonCommercial 4.0 International License

[Click here to view linked References](#)

# Origin of $\{112\}\langle 111\rangle$ antitwinning in a Ti-24Nb-4Zr-8Sn superelastic single crystal

Emmanuel Bertrand<sup>a</sup>, Philippe Castany<sup>b</sup>, Yang Yang<sup>b,c</sup>, Edern Menou<sup>a</sup>, Laurent Couturier<sup>a</sup>,  
Thierry Gloriant<sup>b</sup>

<sup>a</sup> Université de Nantes, CNRS, Institut des Matériaux Jean Rouxel, IMN, F-44000 Nantes,  
France

<sup>b</sup> Univ Rennes, INSA Rennes, CNRS, ISCR – UMR 6226, F-35000 Rennes, France

<sup>c</sup> School of Electromechanical Engineering, Guangdong University of Technology,  
Guangzhou 510006, China

\* Corresponding author: [emmanuel.bertrand@univ-nantes.fr](mailto:emmanuel.bertrand@univ-nantes.fr)

Tel.: +33 2 40 68 31 24

## Abstract

$\{112\}\langle 111\rangle_{\beta}$  twins are observed in a superelastic  $\beta$  Ti-24Nb-4Zr-8Sn (wt.%) single crystal after tensile test. A careful Schmid factor analysis shows that these twins are formed in the antitwinning sense regarding the classical  $\{112\}\langle 111\rangle_{\beta}$  twinning system of bcc structures. These are then  $\{112\}\langle 111\rangle_{\beta}$  antitwins. Moreover, a full stress-induced martensitic (SIM) transformation of  $\beta$  phase into  $\alpha''$  martensite is evidenced from *in situ* synchrotron X-rays diffraction. This transformation is fully accomplished before the onset of plastic deformation and, in turn, the formation of twins. From crystallographic reconstruction,  $\{112\}\langle 111\rangle_{\beta}$  antitwins are shown to be passively formed from the reversion, during the reverse SIM

1 transformation when the stress is released, of  $\{110\}\{110\}_{\alpha''}$  twins actually formed in  $\alpha''$   
2 martensite. The martensitic transformation occurring before twinning plays a key role in the  
3 activation of antitwinning systems by reducing both shear and shuffle magnitudes of  
4 twinning. Variant selection of stress-induced martensite and Schmid factor analysis show that  
5 the classical  $\{112\}\{111\}_{\beta}$  twins can never be activated in  $\beta$  titanium alloys involving SIM  
6 transformation, while the non-classical  $\{112\}\{111\}_{\beta}$  twinning system in the antitwinning  
7 sense is always favored.  
8  
9

10  
11  
12  
13  
14  
15  
16  
17  
18  
19  
20 **Keywords:** Metastable  $\beta$  titanium alloys; Twinning; Antitwinning; Stress-induced martensitic  
21 transformation; Schmid factor analysis.  
22  
23  
24  
25  
26

## 27 **1. Introduction**

28 Metastable  $\beta$  titanium alloys can be designed with highly-biocompatible elements such as Nb,  
29 Ta, Mo, Zr [1-5] and exhibit a low Young's modulus which makes these alloys particularly  
30 suitable for medical applications [6-11]. Numerous deformation mechanisms are known to  
31 operate in metastable  $\beta$  titanium alloys: stress-induced martensitic (SIM) transformation [12-  
32 16], mechanical twinning [17-22] and dislocation slip [23-26]. These deformation  
33 mechanisms lead to peculiar mechanical properties such as superelastic or shape memory  
34 effects [27,12,28-30,13,16,15,14] and transformation induced plasticity (TRIP) or twinning  
35 induced plasticity (TWIP) effects [31-35].  
36  
37  
38  
39  
40  
41  
42  
43  
44  
45  
46  
47  
48

49 SIM transformation occurs from the  $\beta$  phase (bcc) to the  $\alpha''$  phase (C-centered orthorhombic).  
50 It has to be noticed that stress-induced  $\alpha''$  martensite is formed as single untwinned variant in  
51  $\beta$  Ti-based alloys [14,4,18] contrarily to other superelastic alloys such as NiTi alloys wherein  
52 pairs of twinned variants are formed [36-39]. The crystallographic correspondence between  
53 these two phases is given by the modified Burgers Orientation Relationship (BOR):  
54  
55  
56  
57  
58  
59  
60  
61

1  
2  
3  
4  
5  
6  
7  
8  
9  
10  
11  
12  
13  
14  
15  
16  
17  
18  
19  
20  
21  
22  
23  
24  
25  
26  
27  
28  
29  
30  
31  
32  
33  
34  
35  
36  
37  
38  
39  
40  
41  
42  
43  
44  
45  
46  
47  
48  
49  
50  
51  
52  
53  
54  
55  
56  
57  
58  
59  
60  
61  
62  
63  
64  
65

$\{110\}_\beta // (001)_{\alpha''}$  and  $\langle 111 \rangle_\beta // [110]_{\alpha''}$ . Its reversibility generally depends on the metastability of the alloy [40]: a SIM transformation occurring during plastic deformation is no or few reversible and leads to TRIP effect [31-35], while a SIM transformation occurring before plastic deformation is generally highly (completely in the most favourable case) reversible and leads to superelasticity [12,13,41,28,29]. Superelasticity is generally evidenced by the occurrence of a stress plateau on tensile curves followed by a full recovery when the stress is removed. The presence of SIM phase in superelastic alloys can then only be detected under stress due to its reversibility when the stress is released. Residual  $\alpha''$  phase can be observed in highly deformed samples as plasticity impedes the reversion of martensite [42,43], but a full reversible SIM transformation can only be evidenced by *in situ* techniques [12-14,44,15,45].

Observed twinning systems generally have a low magnitude of shear and a low magnitude of shuffle [46]. In body centred cubic (bcc) metals, the operating twinning system is then  $\{112\}\langle 111 \rangle$ . Even if its magnitude of shear is high (0.707 from Tobe et al. [47]), the absence of shuffle makes  $\{112\}\langle 111 \rangle$  twins more favorable in comparison to other theoretical twinning systems with lower magnitude of shear but involving shuffle [46]. It can also be noticed that there is another theoretically predicted twinning system with the same twinning plane and the same twinning direction than the classical  $\{112\}\langle 111 \rangle$  twinning system, which involves a lower value of shear (0.354 from Tobe et al. [47]) but a high magnitude of shuffle [46]. This twinning system with shuffle will be referred as “non-classical”  $\{112\}\langle 111 \rangle$  twinning in the present paper in contrast to the “classical”  $\{112\}\langle 111 \rangle$  system without shuffle. This non-classical system is then unfavourable in comparison with the classical one that not involves any shuffle and is thus not experimentally observed. These two twinning systems share exactly the same twinning plane and shear plane, but share the same twinning direction with a different sense [46]. The classical one is in the twinning sense while the non-

1  
2  
3  
4  
5  
6  
7  
8  
9  
10  
11  
12  
13  
14  
15  
16  
17  
18  
19  
20  
21  
22  
23  
24  
25  
26  
27  
28  
29  
30  
31  
32  
33  
34  
35  
36  
37  
38  
39  
40  
41  
42  
43  
44  
45  
46  
47  
48  
49  
50  
51  
52  
53  
54  
55  
56  
57  
58  
59  
60  
61  
62  
63  
64  
65

classical one lies in the opposite sense, i.e. the antitwinning direction regarding the classical one. The secondary twinning elements are also different between these two systems. All the crystallographic features of these two  $\{112\}\langle 111\rangle$  twinning systems will be detailed in the section 3.4.

The classical  $\{112\}\langle 111\rangle$  twinning system is sometimes observed in metastable  $\beta$  titanium alloys, including TRIP/TWIP [33,34] and superelastic compositions [17], but a peculiar  $\{332\}\langle 113\rangle$  twinning mode is mainly observed in these alloys [17,40,4,20,33,34,19,21,18,22,35]. Classical  $\{112\}\langle 111\rangle$  twins, when observed, are then a secondary and minor twinning mode occurring in addition to preponderant  $\{332\}\langle 113\rangle$  twins [17,33,34].  $\{332\}\langle 113\rangle$  twinning exhibits a much lower magnitude of shear (0.354 from Tobe et al. [47]) than classical  $\{112\}\langle 111\rangle$  twinning but is not observed in other bcc structures due to its high magnitude of shuffle. Occurrence of this peculiar twinning system can be attributed to a low shear modulus in  $\{011\}$  planes along  $\langle 011\rangle$  directions leading to a lattice instability of the bcc structure [47]. This model is consistent with the observation of  $\{332\}\langle 113\rangle$  twins in TWIP and TRIP/TWIP metastable  $\beta$  Ti alloys where no SIM occurs before twinning [33,34,19,48]. However, this explanation cannot be applied to twins in  $\beta$  Ti-based superelastic alloys because a full transformation into SIM  $\alpha''$  phase occurs before twinning. Then,  $\{332\}\langle 113\rangle$  twins clearly result from twinning operations in  $\alpha''$  phase in these alloys. Recent *in situ* characterization of  $\{332\}\langle 113\rangle$  twins in a Ti-27Nb (at.%) showed that superelastic alloys undergo a complex deformation sequence: (1) A full stress-induced martensitic transformation into  $\alpha''$  occurs followed by (2) mechanical twinning of  $\alpha''$  phase and then (3) the reversion into  $\beta$  phase when the stress is released leading to formation of  $\{332\}\langle 113\rangle$  twins [49].  $\{332\}\langle 113\rangle$  twins in  $\beta$  phase are then passively formed from the reversion of twins formerly produced into stress induced  $\alpha''$  martensite. Further observations

1 of transitional structures exhibiting residual  $\alpha''$  martensite along  $\{332\}\langle 113\rangle$  twin boundaries  
2 also support this mechanism of twin reversion [50,51].  
3

4 As twins in  $\beta$  phase can be linked to twins in SIM  $\alpha''$  phase, twinning of  $\alpha''$  phase has to be  
5 considered. Twinning systems of  $\alpha''$  martensite are usually observed in titanium alloys with  
6 initial  $\alpha''$  microstructures.  $\{111\}_{\alpha''}$  type I and  $\langle 211\rangle_{\alpha''}$  type II twinning modes preserve the  
7 orientation of the corresponding  $\beta$  phase by application of the BOR and are then considered as  
8 reorientation twinning systems rather than mechanical ones [27,52,53]. Plastic twinning  
9 systems are also observed in  $\alpha''$  microstructures. The  $\{130\}\langle 310\rangle_{\alpha''}$  system is identified in  
10 some  $\alpha''$  microstructures and its reversion into  $\beta$  phase leads to  $\{332\}\langle 113\rangle_{\beta}$  twins [27,54].  
11  $\{103\}\langle 301\rangle_{\alpha''}$  twins are similarly observed with the same relationship with  $\{332\}\langle 113\rangle_{\beta}$   
12 twins [54].  $\{110\}\langle 110\rangle_{\alpha''}$  twins are also evidenced at the surface of superelastic specimens  
13 [55]. Contrarily to the previous ones, this later twinning system corresponds to the classical  
14  $\{112\}\langle 111\rangle_{\beta}$  twinning system of  $\beta$  phase [56]. Among these twinning systems of  $\alpha''$  phase,  
15  $\{130\}\langle 310\rangle_{\alpha''}$  is the most observed one and was also recently evidenced in TRIP/TWIP  
16 alloys [48]. But clear criterions to explain the activation of twinning systems in  $\alpha''$  are still not  
17 elucidated.  
18

19 This paper focuses on the deformation behavior of a Ti-24Nb-4Zr-8Sn (Ti2448) superelastic  
20 single crystal during a tensile test.  $\{112\}\langle 111\rangle$  mechanical twins are observed in this alloy  
21 after 4.5% of applied strain. Schmid factor analysis will show that these twins correspond to  
22 the non-classical  $\{112\}\langle 111\rangle$  twinning system operating in the antitwinning direction.  
23 Moreover, these antitwins in  $\beta$  phase will be shown to be due to the reversion of twins  
24 occurring in  $\alpha''$  phase. The role of SIM transformation on the observation of  $\{112\}\langle 111\rangle$   
25 antitwins in  $\beta$  phase will be then investigated in terms of twinning shear and shuffle as well as  
26 variant selection of martensite.  
27  
28  
29  
30  
31  
32  
33  
34  
35  
36  
37  
38  
39  
40  
41  
42  
43  
44  
45  
46  
47  
48  
49  
50  
51  
52  
53  
54  
55  
56  
57  
58  
59  
60  
61  
62  
63  
64  
65

## 2. Materials and methods

### 2.1. Experimental methods

A Ti-24Nb-4Zr-8Sn (wt.%) single crystal orientated along a  $\langle 110 \rangle$  direction is used for this study. Experimental details are given in [56]. X-ray diffraction (XRD) Laue back reflection confirmed that the  $\langle 110 \rangle_{\beta}$  direction is obtained within a  $1^{\circ}$  range and the absence of metastable  $\alpha''$  and  $\omega$  phases. Flat tensile specimens with  $3 \times 15 \times 0.5 \text{ mm}^3$  gauge dimensions were machined from the single crystal. An inverse pole figure (IPF) was taken from the single crystal using Electron backscattering diffraction on a Scanning Electron Microscope (SEM-EBSD) and showed that the surface plane of these specimens is  $\{353\}$ . A Jeol JSM 7100F SEM machine working with an accelerating voltage of 20 kV and equipped with a TSL-EBSD system (HKL-Channel 5 analysis software) was used. Specimen was previously prepared with the same procedure than for metallographic observation detailed below. Cyclic tensile tests were conducted at room temperature by strain increments of 0.5% followed by stress release up to an elongation of 5.5% using an INSTRON 3369 tensile machine with a strain rate of  $10^{-4} \text{ s}^{-1}$ . An extensometer was used to ensure the accuracy of strain measurement. Tensile direction (TD) was chosen along the  $\langle 110 \rangle_{\beta}$  direction of the single crystal in order to maximize the transformation strain [57]. A specimen deformed up to 4.5% of applied strain is used for twin characterization. Samples were prepared for metallographic observation by mechanical polishing with increasing grades of SiC abrasive papers, final polishing with colloidal silica suspension and final etching in a solution composed of 8% HF, 15%  $\text{HNO}_3$  and 77%  $\text{H}_2\text{O}$  (vol%). TEM specimens were also cut from tensile specimens and were twin-jet electropolished at 253-263 K in a solution of 6% perchloric acid and 94% methanol (vol. %). Electropolishing was stopped before perforation and final steps of thinning were performed by two-steps ion milling using successively 5 keV

and 1 keV Ar ions with a Fischione 1010 Model. Observations were conducted on a JEOL 2100 microscope operating at 200 kV.

*In situ* synchrotron X-ray diffraction (SXR) during cyclic tensile test was conducted on beam line ID31 at the European Synchrotron Radiation Facility (ESRF, Grenoble, France) with a 5 kN micro-tensile machine. The high-resolution ID31 beamline offers a high-energy incident X-ray beam ( $\lambda = 0.040002106$  nm) coupled with a nine-channel multi-analyzer detector. The transmitted diffracted beams were collected over the  $2\theta$  angular range  $4\text{--}28^\circ$  with a scanning step of  $0.005^\circ$ . The *in situ* cyclic tensile test under synchrotron radiation was realized on a single crystal specimen with the same geometry than for tensile tests (gauge width of 3 mm and thickness of 0.5 mm) with strain increments of 0.5 % until 5.5 %. SXR scans were therefore obtained after each strain increment for both loading and unloading conditions. More details can be found in [56,12].

## 2.2. Variant selection

Each variant of  $\alpha''$  martensite can be obtained from  $\beta$  phase orientation by application of BOR. The transformation of a  $\beta$  crystal into  $\alpha''$  martensite leads to 6 equivalent lattice correspondence variants (CV) given in Table 1. Under uniaxial applied stress, activated variants are expected to be the ones leading to the highest transformation strain along the stress direction [53,58,57].

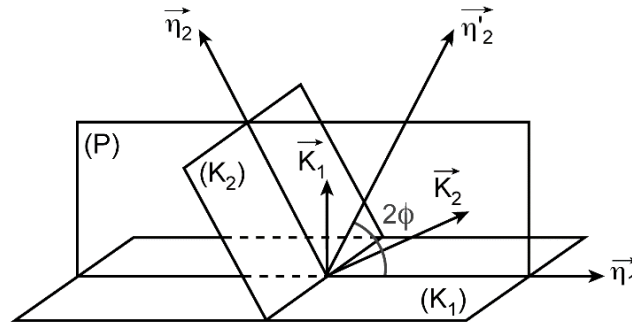
Table 1. Lattice correspondence variants (CV) derived from  $\beta$  and  $\alpha''$  crystals and transformation lattice strain of each CV along the  $[101]_\beta$  tensile axis.

Variant	$[100]_{\alpha''}$	$[010]_{\alpha''}$	$[001]_{\alpha''}$	Strain
CV1	$[100]_\beta$	$[011]_\beta$	$[0\bar{1}1]_\beta$	1.51%
CV2	$[100]_\beta$	$[0\bar{1}1]_\beta$	$[01\bar{1}]_\beta$	1.51%
CV3	$[010]_\beta$	$[101]_\beta$	$[10\bar{1}]_\beta$	4.31%
CV4	$[010]_\beta$	$[10\bar{1}]_\beta$	$[\bar{1}0\bar{1}]_\beta$	3.99%
CV5	$[001]_\beta$	$[110]_\beta$	$[\bar{1}10]_\beta$	1.51%
CV6	$[001]_\beta$	$[\bar{1}10]_\beta$	$[\bar{1}\bar{1}0]_\beta$	1.51%

1  
2 Twinning systems are usually described by their twinning elements:  $K_1$ ,  $\eta_1$ ,  $K_2$ ,  $\eta_2$  and P [46]  
3  
4 as shown on Fig 1. Variant selection during mechanical twinning of  $\beta$  and  $\alpha''$  phases can be  
5  
6 determined using a Schmid factor analysis adapted to this deformation mechanism [17,27].  
7  
8 Schmid factor, written  $m$ , is defined similarly to slip as:  
9

$$m = \cos \lambda \cos \varphi$$

10  
11  
12 where  $\lambda$  is the angle between tensile direction (TD) and  $\overline{K_1}$  and  $\phi$  the angle between TD and  
13  
14  $\overline{\eta_1}$ . Contrarily to dislocation slip, values of  $\lambda$  and  $\phi$  are taken between  $0^\circ$  and  $180^\circ$  in order to  
15  
16 obtain  $m$  values ranging between -0.5 and 0.5. Using this convention, a twin variant can be  
17  
18 activated in tension if its associated Schmid factor is positive. The sign of  $m$  plays then a key  
19  
20 role in the present study. So, signs of  $K_1$  and  $\eta_1$  have to be chosen carefully with respect to  
21  
22 Fig. 1, as detailed in Appendix A of [27]. Twinning elements of each system are identified in  
23  
24 section 3.4.  
25  
26  
27  
28  
29  
30



31  
32  
33  
34  
35  
36  
37  
38  
39  
40  
41  
42  
43  
44  
45  
46 Fig. 1 The four twinning elements contained in the shear plane (P).  
47  
48  
49

50  
51 In the present study, two twinning systems for each phase will be considered:  $\{112\}\langle 111 \rangle_\beta$   
52  
53 and  $\{110\}\langle 110 \rangle_{\alpha''}$ . This notation without minus sign in index of  $\eta_1$  will be used for the  
54  
55 generic denomination of each system. Conversely, signs will be specified when the twinning  
56  
57 (t) or the antitwinning (at) sense will be considered:  $\{112\}\langle \bar{1}\bar{1}1 \rangle_\beta^t$  and  $\{110\}\langle 1\bar{1}0 \rangle_{\alpha''}^t$   
58  
59  
60  
61  
62  
63  
64  
65

1 correspond then to twinning systems when the sign of  $\eta_1$  indicates the twinning sense and  
2  $\{112\}\langle 11\bar{1}\rangle_{\beta}^{at}$  and  $\{110\}\langle \bar{1}10\rangle_{\alpha'}^{at}$ , correspond to twinning systems when the sign of  $\eta_1$   
3  
4 corresponds to the antitwinning sense. In this paper, the twinning sense is always defined as  
5 the twinning direction of the classical twinning system of bcc structures, whatever the phase  
6  
7 considered.  
8  
9  
10

### 11 **3. Results and discussion**

#### 12 **3.1. Preliminary results: tensile tests and *in situ* SXR D characterization**

13  
14  
15  
16  
17  
18  
19  
20  
21  
22  
23  
24  
25  
26  
27  
28  
29  
30  
31  
32  
33  
34  
35  
36  
37  
38  
39  
40  
41  
42  
43  
44  
45  
46  
47  
48  
49  
50  
51  
52  
53  
54  
55  
56  
57  
58  
59  
60  
61  
62  
63  
64  
65  
The main experimental results are summarized in this section. A full description of phase transformations and mechanical behavior of the present Ti2448 single crystal is available in a previous study [56]. Fig. 2a shows the cyclic tensile curve of the  $[101]_{\beta}$  single crystal strained from 0 to 5.5% and the corresponding *in situ* SXR D diffraction profiles under stress (Fig 2b) and when the stress is removed (Fig 2c). The  $(110)_{\beta}$  peak is represented by black circles in SXR D profiles, while  $(002)_{\alpha'}$ ,  $(111)_{\alpha'}$  and  $(020)_{\alpha'}$  peaks of martensite are labeled with white circles, black squares and stars, respectively. A stress plateau is observed from 0.7% to 3% of applied strain on the tensile curve and corresponds to SIM transformation as shown in SXR D patterns (Fig 2b). From 4.5% of applied strain, no more  $\beta$  phase is detected on loading, highlighting a full SIM transformation.  $\alpha'$  phase disappears and  $\beta$  phase is restored upon unloading until a strain of 4%. Irreversible strain is observed from 4.5% only and residual  $\alpha'$  phase is observed upon unloading. These observations support that plastic deformation mechanisms such as dislocation glide and mechanical twinning do not occur extensively below this strain level.

Finally, the key feature for the present paper is that a full martensitic transformation from  $\beta$  phase to  $\alpha'$  phase is observed on loading, which means that when plastic deformation occurs, the microstructure is only composed of  $\alpha'$  martensite.

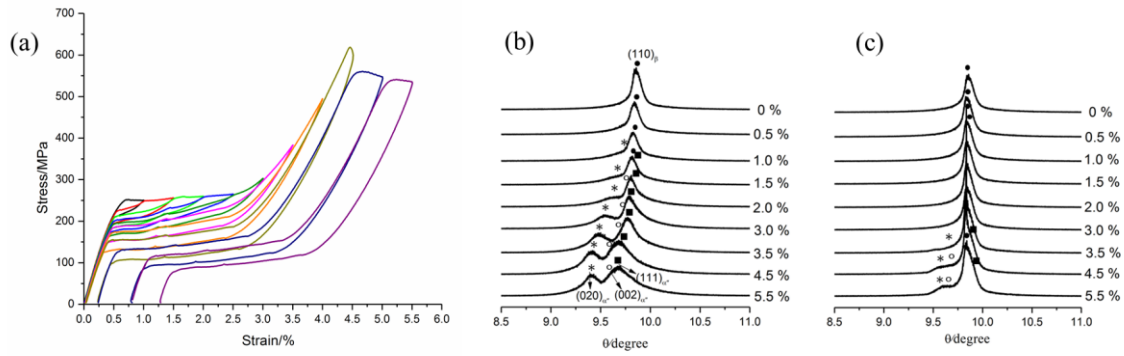


Fig. 2 Cyclic tensile curve of the Ti-24Nb-4Zr-8Sn single crystal (a). *In situ* synchrotron X-ray diffraction profiles during a cyclic tensile test on loading (b) and after unloading (c); black circles correspond to  $(110)_{\beta}$  peak, white circles to  $(002)_{\alpha'}$ , black squares to  $(111)_{\alpha''}$  and stars to  $(020)_{\alpha''}$ .

### 3.2. Deformation sequence

It has first to be noted that Schmid factor analysis is required to distinguish the twinning direction from the antitwinning direction of observed twins. In this section, twinning systems are then labeled without signs and twinning/antitwinning directions will be determined in section 3.3.

The microstructure of the Ti2448 single crystal after 4.5% strain is first investigated by optical microscopy. As the single crystal is observed after unloading and according to SXRD results, most of the martensite is reversed into  $\beta$  phase. Fig. 3a shows that two orientations of twins cross the single crystal. These twins were previously characterized by TEM observations and identified as  $\{112\}\langle 111 \rangle_{\beta}$  twins with the presence of a thin layer of interfacial  $\omega$  phase along the twin boundaries [56]. Another example of such a twin is shown on the Fig. 3b. The corresponding diffraction pattern in Fig. 3c is taken along a  $\langle 110 \rangle$  zone axis which is common to both  $\beta$  matrix and  $\{112\}\langle 111 \rangle_{\beta}$  twin. Typical spots of a single variant of  $\omega$  phase are also clearly visible. As formerly reported, this single variant of  $\omega$  phase

lies at the twin interface and impedes any direct observation of its atomic structure [56]. Some dislocations are also visible in Fig. 3b. Both dislocation glide and  $\{112\}\langle 111 \rangle_{\beta}$  twinning are then activated during plastic deformation.

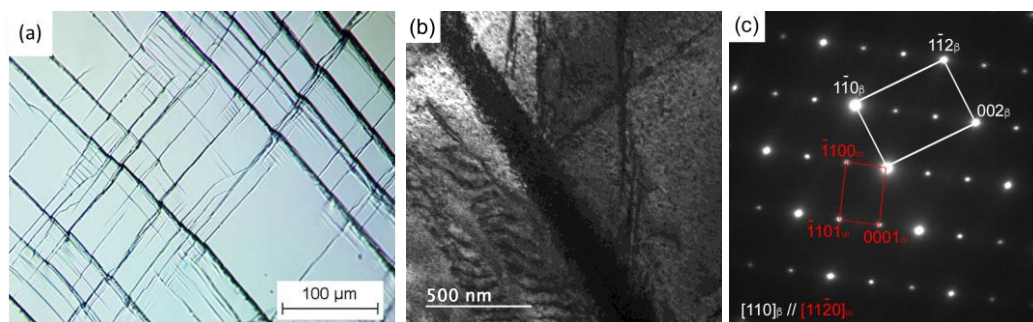


Fig. 3 Optical micrograph of the Ti-24Nb-4Zr-8Sn single crystal after being strained up to 4.5% (a) and TEM observation of a twin (b) and corresponding diffraction pattern showing the presence of interfacial twin boundary  $\omega$  phase (c).

As mechanical twinning involves unrecoverable plastic deformation, it must occur beyond 4% of strain, i.e. when the microstructure is only composed of  $\alpha''$  martensite. As a consequence, twinning actually occurs in  $\alpha''$  phase according to the  $\{110\}\langle 110 \rangle_{\alpha''}$  twinning system as previously evidenced [56]. The deformation sequence can thus be summarized as shown on Fig. 4. After elastic deformation of the  $\beta$  phase, when the strain is increasing:

- $\beta$  phase is first transformed into stress-induced  $\alpha''$  martensite. Transformation strain along TD is calculated for each possible CV of martensite (Table 1) and leads to the variant selection of CV3, which gives the highest value of transformation strain.

- At higher strain, twinning and dislocation glide of  $\alpha''$  phase occur. According to [56],  $\{110\}\langle 110 \rangle_{\alpha''}$  twins are formed into martensite.

- Then, when the stress is removed, the parent crystal and twins reverse each into  $\beta$  phase, leading to the presence of  $\{112\}\langle 111 \rangle_{\beta}$  twins into  $\beta$  phase.

As a conclusion, the observed  $\{112\}\langle 111 \rangle_{\beta}$  twins actually correspond to the reversion during reverse SIM transformation of  $\{110\}\langle 110 \rangle_{\alpha''}$  twins activated into the stress-induced  $\alpha''$  martensite.

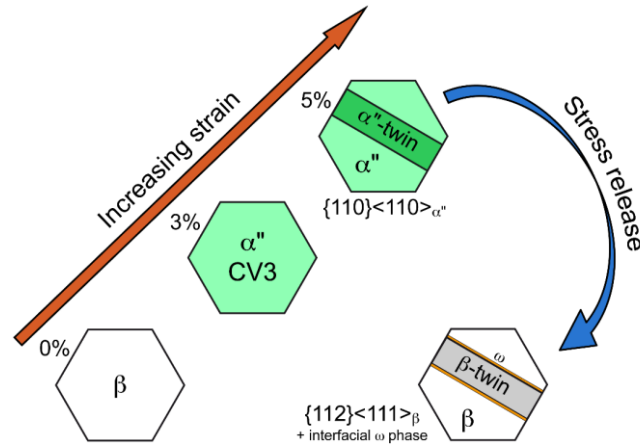


Fig. 4 Deformation sequence of the Ti-24Nb-4Zr-8Sn single crystal under loading and after unloading.

### 3.3. Schmid factor analysis and twinning system identification

Fig. 5a represents the stereographic projection corresponding to the  $\beta$  phase single crystal orientation where the TD is chosen as  $[101]_{\beta}$  and the surface plane is  $(\bar{3}\bar{5}3)_{\beta}$  as specified in section 2.1. Using this convention, CV3 is expected to be formed under stress (Table 1). Fig. 5b is then the stereographic projection of the corresponding  $\alpha''$  single crystal obtained by application of the  $\beta/\alpha''$  orientation relationship for the CV3. This orientation of  $\alpha''$  phase is assumed to be the parent crystal orientation with TD along the  $[010]_{\alpha''}$  direction when twins are activated.

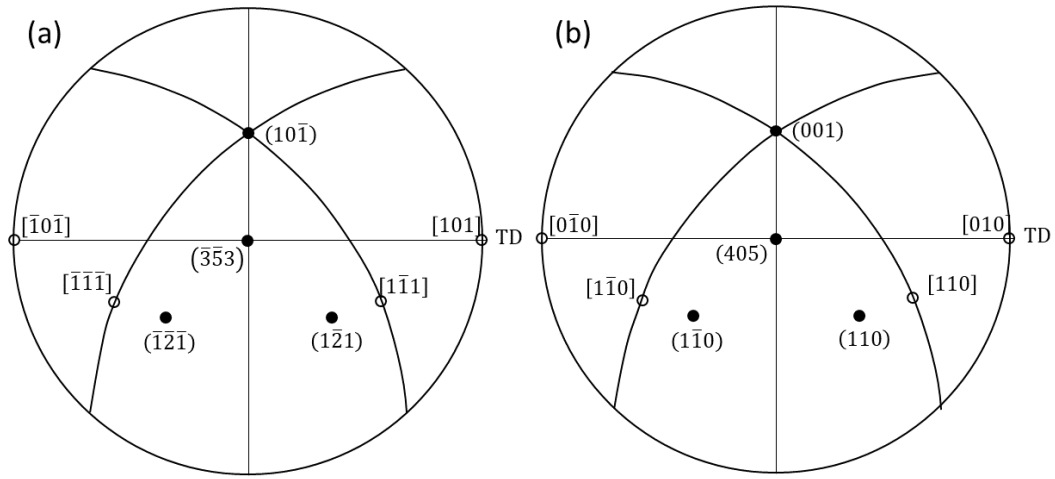


Fig. 5 Stereographic projections with respect to the orientation of Fig 3(a):  $\beta$  phase (a) and stress induced  $\alpha''$  martensite CV3 (b).

The notation of each twin variant is summarized in Table 2. For each variant, the twinning plane  $K_1$  is given, as well as the index of  $\eta_1$  along the twinning direction ( $\eta_{1t}$ ) or along the antitwining direction in the opposite sense ( $\eta_{1at}$ ). There are 12 twin variants in  $\beta$  phase and 2 variants in  $\alpha''$  phase due to their respective symmetry. Comparison of twins orientations in Fig. 3a and traces of  $\{112\}_\beta$  planes in Fig. 5a shows that the observed twins in  $\beta$  phase corresponds to  $V2_\beta$  and  $V8_\beta$  twin variants. Moreover, traces of  $\{112\}_\beta$  twinning planes corresponding to  $V2_\beta$  and  $V8_\beta$  twin variants correspond exactly to the traces of  $\{110\}_{\alpha''}$  planes of both variants of  $\{110\}\langle 110 \rangle_{\alpha''}$  twins in the CV3 of  $\alpha''$  martensite. This point confirms that the CV3 of martensite is the one really formed during deformation as expected from calculations of transformation strains. Indeed, if another CV of martensite was formed, the positions of  $\{110\}_{\alpha''}$  planes would be different and would correspond to two other  $\{112\}_\beta$  planes whom traces will have different orientations than the ones observed on the optical micrograph.

Table 2. Principal twinning elements of the 12 variants of  $\{112\}\langle 111 \rangle_{\beta}$  and 2 variants of  $\{110\}\langle 110 \rangle_{\alpha''}$  considering the twinning sense  $\eta_{1t}$  and antitwinning sense  $\eta_{1at}$ .

Variant	$K_1$	$\eta_{1t}$	$\eta_{1at}$
V1 $_{\beta}$	(112)	$[\bar{1}\bar{1}1]$	$[1\bar{1}\bar{1}]$
V2 $_{\beta}$	(121)	$[\bar{1}\bar{1}\bar{1}]$	$[1\bar{1}\bar{1}]$
V3 $_{\beta}$	(211)	$[1\bar{1}\bar{1}]$	$[\bar{1}11]$
V4 $_{\beta}$	( $\bar{1}$ 12)	$[1\bar{1}\bar{1}]$	$[\bar{1}\bar{1}\bar{1}]$
V5 $_{\beta}$	( $\bar{1}$ 21)	$[1\bar{1}\bar{1}]$	$[\bar{1}\bar{1}\bar{1}]$
V6 $_{\beta}$	( $\bar{2}$ 11)	$[\bar{1}\bar{1}\bar{1}]$	$[111]$
V7 $_{\beta}$	(1 $\bar{1}$ 2)	$[\bar{1}\bar{1}\bar{1}]$	$[1\bar{1}\bar{1}]$
V8 $_{\beta}$	( $\bar{1}$ 2 $\bar{1}$ )	$[\bar{1}\bar{1}\bar{1}]$	$[111]$
V9 $_{\beta}$	(2 $\bar{1}$ 1)	$[1\bar{1}\bar{1}]$	$[\bar{1}\bar{1}\bar{1}]$
V10 $_{\beta}$	(11 $\bar{2}$ )	$[\bar{1}\bar{1}\bar{1}]$	$[111]$
V11 $_{\beta}$	(12 $\bar{1}$ )	$[\bar{1}\bar{1}\bar{1}]$	$[1\bar{1}\bar{1}]$
V12 $_{\beta}$	(21 $\bar{1}$ )	$[1\bar{1}\bar{1}]$	$[\bar{1}\bar{1}\bar{1}]$
V1 $_{\alpha''}$	(110)	$[1\bar{1}0]$	$[\bar{1}10]$
V2 $_{\alpha''}$	( $\bar{1}$ 10)	$[\bar{1}\bar{1}0]$	$[110]$

Schmid factor analysis is used considering both twinning and antitwinning systems for  $\beta$  and  $\alpha''$  phases:  $\{112\}\langle \bar{1}\bar{1}1 \rangle_{\beta}^t$  and  $\{112\}\langle 11\bar{1} \rangle_{\beta}^{at}$ ;  $\{110\}\langle 1\bar{1}0 \rangle_{\alpha''}^t$  and  $\{110\}\langle \bar{1}10 \rangle_{\alpha''}^{at}$  (Table 3). Of course, values of Schmid factors for twinning direction ( $m_t$ ) have the same absolute values than for antitwinning direction ( $m_{at}$ ), only the sign is opposite.

Table 3. Schmid factors of the 12 variants of  $\{112\}\langle \bar{1}\bar{1}1 \rangle_{\beta}^t$  and  $\{112\}\langle 11\bar{1} \rangle_{\beta}^{at}$  for a  $[101]_{\beta}$  tensile direction and the 2 variants of  $\{110\}\langle 1\bar{1}0 \rangle_{\alpha''}^t$  and  $\{110\}\langle \bar{1}10 \rangle_{\alpha''}^{at}$  for a  $[010]_{\alpha''}$  tensile direction.

Variant	$m_t$	$m_{at}$
V1 $_{\beta}$	0,000	0,000
V2 $_{\beta}$	-0,471	0,471
V3 $_{\beta}$	0,000	0,000
V4 $_{\beta}$	0,236	-0,236
V5 $_{\beta}$	0,000	0,000
V6 $_{\beta}$	0,236	-0,236
V7 $_{\beta}$	0,000	0,000
V8 $_{\beta}$	-0,471	0,471
V9 $_{\beta}$	0,000	0,000
V10 $_{\beta}$	0,236	-0,236
V11 $_{\beta}$	0,000	0,000
V12 $_{\beta}$	0,236	-0,236
V1 $_{\alpha''}$	-0,463	0,463
V2 $_{\alpha''}$	-0,463	0,463

1 As the observed twins are obtained during a tensile test, activated variants are expected to  
 2 have a high and positive  $m$  value. However, the observed  $V2_\beta$  and  $V8_\beta$  variants have  
 3  
 4 surprisingly a negative  $m$  value with high absolute values, close to -0.5 when  $\{112\}\langle\bar{1}\bar{1}1\rangle_\beta^t$  is  
 5  
 6 considered. Therefore, the consideration of the classical  $\{112\}\langle\bar{1}\bar{1}1\rangle_\beta^t$  twinning system, i.e.  
 7  
 8 twinning in the twinning sense, leads to an apparently incoherent result with observed twins  
 9  
 10 corresponding to a compression of the crystal.  
 11  
 12

13  
 14 As the positions of  $\{110\}_{\alpha''}$  planes and  $\langle 110 \rangle_{\alpha''}$  directions of  $V2_{\alpha''}$  and  $V1_{\alpha''}$  are very close  
 15  
 16 to  $\{112\}_\beta$  planes and  $\langle 111 \rangle_\beta$  directions of  $V2_\beta$  and  $V8_\beta$  respectively (Fig. 5a and 5b), similar  
 17  
 18  $m$  values close to -0.5 are also found for  $\{110\}\langle 1\bar{1}0 \rangle_{\alpha''}^t$  twinning (Table 3). Whatever  $\beta$  or  $\alpha''$   
 19  
 20 phase is considered, Schmid factor calculations for twin variants in the twinning sense ( $m_t$ )  
 21  
 22 show that the observed twin variants lead to a compression of the single crystal along its  
 23  
 24 tensile direction. This is of course not observed as the single crystal is elongated during the  
 25  
 26 present tensile test. Therefore,  $\{112\}\langle\bar{1}\bar{1}1\rangle_\beta^t$  or  $\{110\}\langle 1\bar{1}0 \rangle_{\alpha''}^t$  twins cannot be activated. This  
 27  
 28 means that the observed twins are not the classical  $\{112\}\langle 111 \rangle_\beta$  twinning system of bcc  
 29  
 30 structures, and, in turn, are the non-classical  $\{112\}\langle 11\bar{1} \rangle_\beta^{at}$  twinning system with a shear in  
 31  
 32 the antitwinning sense regarding the classical  $\{112\}\langle 111 \rangle_\beta$  mode. If twinning is then  
 33  
 34 considered to occur in the antitwinning sense but in the same plane, Schmid factors ( $m_{at}$ ) will  
 35  
 36 have high and positive values for the observed twin variants (Table 3). Considering the  
 37  
 38 activation of this non-classical  $\{112\}\langle 11\bar{1} \rangle_\beta^{at}$  system, the crystal will be elongated along the  
 39  
 40 tensile direction with the two observed twin variants. Therefore, this careful Schmid factor  
 41  
 42 analysis allows to determine that the observed  $\{112\}\langle 111 \rangle_\beta$  twins does not correspond to the  
 43  
 44 classical twinning mode of bcc structures but to the non-classical  $\{112\}\langle 11\bar{1} \rangle_\beta^{at}$  twinning  
 45  
 46 system shearing in the antitwinning sense.  $\{112\}\langle 111 \rangle_\beta$  twinning in the antitwinning sense  
 47  
 48  
 49  
 50  
 51  
 52  
 53  
 54  
 55  
 56  
 57  
 58  
 59  
 60  
 61  
 62  
 63  
 64  
 65

was never observed, as its activation energy is much higher than the one in the twinning sense due to a much higher value of atomic shuffle as detailed in the next section.

### 3.4. Twinning elements

As stated in the introduction, the classical  $\{112\}\langle\bar{1}\bar{1}1\rangle_{\beta}^t$  mode and the non-classical  $\{112\}\langle11\bar{1}\rangle_{\beta}^{at}$  mode in the antitwinning sense have the same principal twinning elements but different secondary twinning elements. Consequently, the same feature will be found for twinning systems in  $\alpha''$  phase due to the orientation relationship between  $\beta$  and  $\alpha''$  phases.

Table 4. Twinning elements for twinning systems in the twinning and antitwinning senses in  $\beta$  and  $\alpha''$  phases and associated shear (s) and shuffle magnitudes.

Twinning system	$K_1$	$\eta_1$	$K_2$	$\eta_2$	P	s	shuffle magnitude
$\{112\}\langle\bar{1}\bar{1}1\rangle_{\beta}^t$	(121)	$[\bar{1}\bar{1}\bar{1}]$	$(\bar{1}2\bar{1})$	[111]	(10 $\bar{1}$ )	0.707	0
$\{112\}\langle11\bar{1}\rangle_{\beta}^{at}$	(121)	[1 $\bar{1}\bar{1}$ ]	(3 $\bar{2}$ 3)	[131]	(10 $\bar{1}$ )	0.354	1/2 [1 $\bar{1}$ 1]
$\{110\}\langle1\bar{1}0\rangle_{\alpha''}^t$	(110)	[1 $\bar{1}$ 0]	(1 $\bar{1}$ 0)	[110]	(001)	0.821	1/5 [1 $\bar{1}$ 0]
$\{110\}\langle\bar{1}10\rangle_{\alpha''}^{at}$	(110)	$[\bar{1}10]$	$(\bar{1}30)$	[310]	(001)	0.259	1/5 $[\bar{1}10]$

Principal and secondary twinning elements of each twinning system can be calculated using the Bilby and Crocker theory and can be found in the following references for  $\{112\}\langle\bar{1}\bar{1}1\rangle_{\beta}^t$  and  $\{112\}\langle11\bar{1}\rangle_{\beta}^{at}$  [46,47] and for  $\{110\}\langle1\bar{1}0\rangle_{\alpha''}^t$  and  $\{110\}\langle\bar{1}10\rangle_{\alpha''}^{at}$  [55]. These elements are given in Table 4 for each considered twinning system and in Table 5 for each twin variant. As each twinning element is commensurable, these twinning systems are all of compound type. Fig. 6 shows these twinning elements on stereographic projections in  $\beta$  phase (Fig. 6a) and in  $\alpha''$  phase (Fig. 6b) and the associated dichromatic diagrams with respect of the orientation relationship in  $\beta$  phase (Fig. 6c) and  $\alpha''$  phase (Fig. 6d). The pole of  $K_1$  is on the top of the stereographic projections and the pole of the shear plane P is normal to the surface of projections.  $\eta_1$  directions of the  $\beta$  and  $\alpha''$  twinning systems point both to the right of the

projections whereas  $\eta_1$  directions of antitwinning systems point to the left. Secondary twinning elements  $K_2$  and  $\eta_2$  are also shown on these figures for each system. Shear values are calculated using the formula  $s = 2\cotan(2\phi)$  where  $\phi$  is the angle between  $\eta_1$  and the secondary twinning direction in the twinned crystal  $\eta_2'$  (Fig. 1).

Table 5. Twinning elements of the 12 variants of  $\{112\}\langle\bar{1}\bar{1}\bar{1}\rangle_\beta^t$ ,  $\{112\}\langle 11\bar{1}\rangle_\beta^{at}$  and the 2 variants of  $\{110\}\langle\bar{1}\bar{1}0\rangle_{\alpha''}^t$  and  $\{110\}\langle\bar{1}\bar{1}0\rangle_{\alpha''}^{at}$ .

	$K_1$	$\eta_1$	$K_2$	$\eta_2$		$K_1$	$\eta_1$	$K_2$	$\eta_2$
$V1_\beta^t$	(112)	$[\bar{1}\bar{1}\bar{1}]$	$(\bar{1}\bar{1}\bar{2})$	[111]	$V1_\beta^{at}$	(112)	$[11\bar{1}]$	$(33\bar{2})$	[113]
$V2_\beta^t$	(121)	$[\bar{1}\bar{1}\bar{1}]$	$(\bar{1}\bar{2}\bar{1})$	[111]	$V2_\beta^{at}$	(121)	$[1\bar{1}\bar{1}]$	$(3\bar{2}3)$	[131]
$V3_\beta^t$	(211)	$[\bar{1}\bar{1}\bar{1}]$	$(2\bar{1}\bar{1})$	[111]	$V3_\beta^{at}$	(211)	$[\bar{1}\bar{1}\bar{1}]$	$(\bar{2}33)$	[311]
$V4_\beta^t$	$(\bar{1}\bar{1}\bar{2})$	$[1\bar{1}\bar{1}]$	$(1\bar{1}\bar{2})$	$[\bar{1}\bar{1}\bar{1}]$	$V4_\beta^{at}$	$(\bar{1}\bar{1}\bar{2})$	$[\bar{1}\bar{1}\bar{1}]$	$(\bar{3}\bar{3}\bar{2})$	$[\bar{1}\bar{1}\bar{3}]$
$V5_\beta^t$	$(\bar{1}\bar{2}\bar{1})$	$[11\bar{1}]$	$(12\bar{1})$	$[\bar{1}\bar{1}\bar{1}]$	$V5_\beta^{at}$	$(\bar{1}\bar{2}\bar{1})$	$[\bar{1}\bar{1}\bar{1}]$	$(\bar{3}\bar{2}3)$	$[\bar{1}\bar{3}\bar{1}]$
$V6_\beta^t$	$(\bar{2}\bar{1}\bar{1})$	$[\bar{1}\bar{1}\bar{1}]$	$(\bar{2}\bar{1}\bar{1})$	$[\bar{1}\bar{1}\bar{1}]$	$V6_\beta^{at}$	$(\bar{2}\bar{1}\bar{1})$	[111]	(233)	$[\bar{3}\bar{1}\bar{1}]$
$V7_\beta^t$	$(1\bar{1}\bar{2})$	$[\bar{1}\bar{1}\bar{1}]$	$(\bar{1}\bar{1}\bar{2})$	$[1\bar{1}\bar{1}]$	$V7_\beta^{at}$	$(1\bar{1}\bar{2})$	$[1\bar{1}\bar{1}]$	$(3\bar{3}\bar{2})$	$[1\bar{1}\bar{3}]$
$V8_\beta^t$	$(1\bar{2}\bar{1})$	$[\bar{1}\bar{1}\bar{1}]$	$(\bar{1}\bar{2}\bar{1})$	$[1\bar{1}\bar{1}]$	$V8_\beta^{at}$	$(1\bar{2}\bar{1})$	[111]	(323)	[131]
$V9_\beta^t$	$(2\bar{1}\bar{1})$	$[11\bar{1}]$	$(21\bar{1})$	$[1\bar{1}\bar{1}]$	$V9_\beta^{at}$	$(2\bar{1}\bar{1})$	$[\bar{1}\bar{1}\bar{1}]$	$(\bar{2}\bar{3}\bar{3})$	$[3\bar{1}\bar{1}]$
$V10_\beta^t$	$(11\bar{2})$	$[\bar{1}\bar{1}\bar{1}]$	$(\bar{1}\bar{1}\bar{2})$	$[1\bar{1}\bar{1}]$	$V10_\beta^{at}$	$(11\bar{2})$	[111]	(332)	[113]
$V11_\beta^t$	$(12\bar{1})$	$[\bar{1}\bar{1}\bar{1}]$	$(\bar{1}\bar{2}\bar{1})$	$[1\bar{1}\bar{1}]$	$V11_\beta^{at}$	$(12\bar{1})$	$[1\bar{1}\bar{1}]$	$(3\bar{2}\bar{3})$	[131]
$V12_\beta^t$	$(21\bar{1})$	$[1\bar{1}\bar{1}]$	$(2\bar{1}\bar{1})$	$[1\bar{1}\bar{1}]$	$V12_\beta^{at}$	$(21\bar{1})$	$[\bar{1}\bar{1}\bar{1}]$	$(\bar{2}\bar{3}\bar{3})$	[311]
$V1_{\alpha''}^t$	(110)	$[\bar{1}\bar{1}0]$	$(\bar{1}\bar{1}0)$	[110]	$V1_{\alpha''}^{at}$	(110)	$[\bar{1}\bar{1}0]$	$(\bar{1}30)$	[310]
$V2_{\alpha''}^t$	$(\bar{1}\bar{1}0)$	$[\bar{1}\bar{1}0]$	$(\bar{1}\bar{1}0)$	$[\bar{1}\bar{1}0]$	$V2_{\alpha''}^{at}$	$(\bar{1}\bar{1}0)$	[110]	(130)	$[\bar{3}\bar{1}0]$

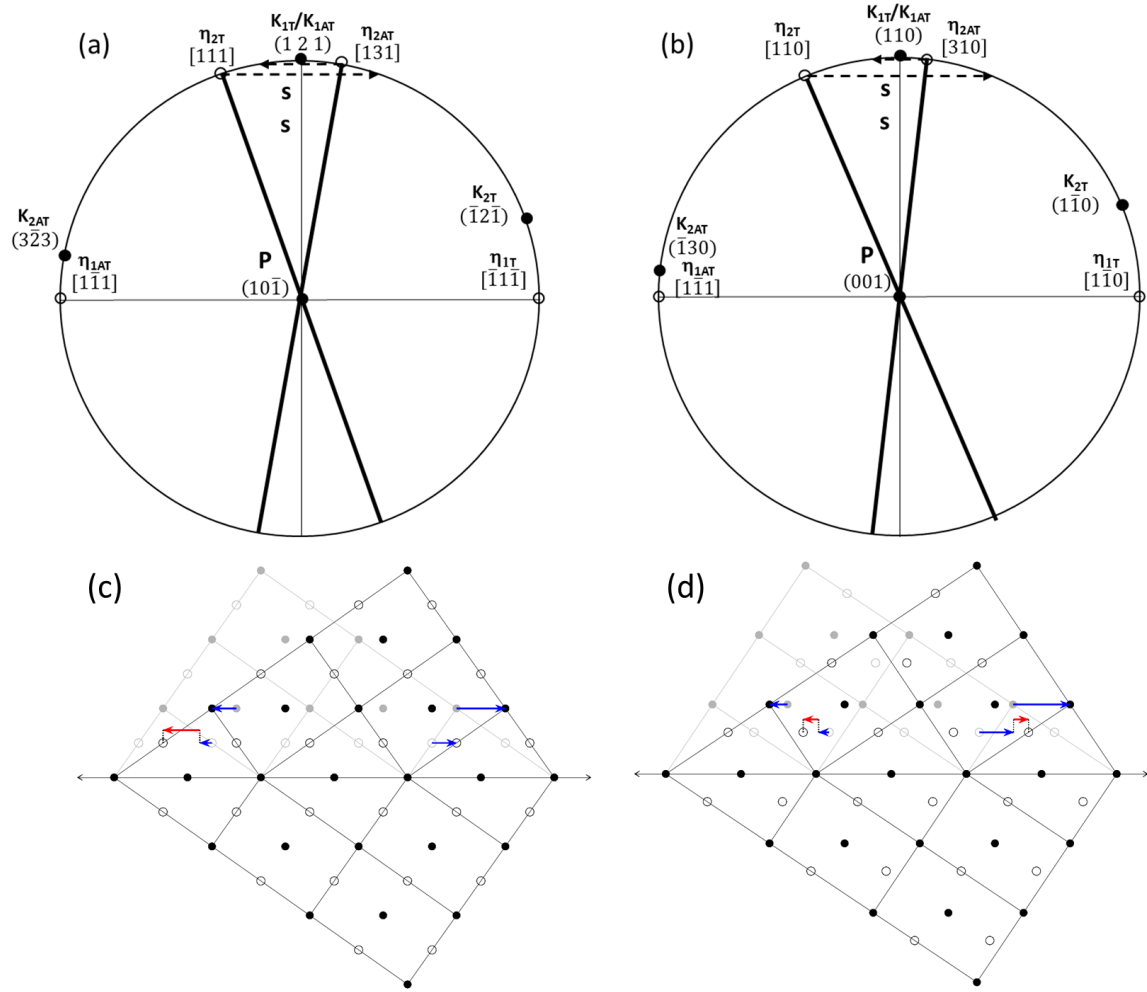


Fig. 6 Stereographic projections showing twinning (T in subscript) and antitwinning (AT in subscript) elements for  $\beta$  phase (a) and  $\alpha''$  phase (b) and associated dichromatic diagrams (c and d, respectively). Filled circles correspond to atoms in the plane of the figure and empty circles correspond to atoms above the plane of the figure.

As it is acknowledged that activated twinning systems exhibit low shear and shuffle [46,47], dichromatic diagrams of  $\beta$  and  $\alpha''$  phases are used to highlight shear and shuffle values of each twinning system (Fig. 6c and Fig. 6d). Twinning direction points to the right and antitwinning direction points to the left. The obtained shear and shuffle values are summarized in Table 4. They are measured as follows:

1  
2  
3  
4  
5  
6  
7  
8  
9  
10  
11  
12  
13  
14  
15  
16  
17  
18  
19  
20  
21  
22  
23  
24  
25  
26  
27  
28  
29  
30  
31  
32  
33  
34  
35  
36  
37  
38  
39  
40  
41  
42  
43  
44  
45  
46  
47  
48  
49  
50  
51  
52  
53  
54  
55  
56  
57  
58  
59  
60  
61  
62  
63  
64  
65

- the plane located two atomic layers above the twinning plane of the figure is assumed to undergo simple shear during the twinning operation. This necessary shear is applied to the whole twinned crystal and is represented by blue arrows on Fig 6c and Fig 6d;

- the plane located one atomic layer above the twinning plane needs additional shuffle to reach the twinning configuration. This shuffle, represented by red arrows, is applied to every white atom of Fig 6c and Fig 6d.

Shuffle is an important parameter to take into account to explain twinning of bcc structures.

Whereas shear of  $\{112\}\langle 11\bar{1}\rangle_{\beta}^{at}$  is very low, this system is generally not activated in bcc structures due to its high shuffle magnitude ( $1/2 [1\bar{1}1]$ ). Conversely, no shuffle is necessary for classical  $\{112\}\langle \bar{1}\bar{1}1\rangle_{\beta}^t$ , making it easier to activate in spite of its higher shear value [46].

The case of  $\alpha''$  phase is more complex because several dichromatic diagrams can be obtained from its twinning elements due to its double-layered structure. Investigation by high resolution transmission electron microscopy may reveal the real structure of the  $\alpha''$  twin interface. But this phase disappears when the stress is released and makes this kind of observation difficult. Several configurations were then tested and the most probable configuration, i.e. the one with minimal shear and shuffle magnitudes, is shown on Fig 6d. In this condition, the shear is lower for  $\{110\}\langle \bar{1}10\rangle_{\alpha''}^{at}$ , than for  $\{110\}\langle 1\bar{1}0\rangle_{\alpha''}^t$ , and the atomic shuffle is the same for both twinning systems. Thus,  $\{110\}\langle \bar{1}10\rangle_{\alpha''}^{at}$  is easier to activate thanks to its low shear and low shuffle magnitudes. Then, as the shuffle value is the same for twinning and antitwinning direction in  $\alpha''$  phase, the twinning direction has to be the one involving the lowest shear. As a consequence, twinning and antitwinning senses are inverted in  $\alpha''$  phase in comparison with  $\beta$  phase.

Finally, observation of twins in the antitwinning sense in  $\beta$  phase is due to the activation of twins in SIM  $\alpha''$  because of lower shear in the antitwinning sense than in the twinning sense

1 of the prior  $\beta$  phase. In other words, it was firstly assumed that twinning senses are the same  
2 in both  $\beta$  and  $\alpha''$  phases, while not. Consequently, what is denoted “antitwinning” in  $\alpha''$  phase  
3 actually corresponds to twinning sense in this phase, but corresponds to antitwinning sense in  
4  $\beta$  phase. Despite this, subscripts (t) and (at) in the notation of twinning systems in  $\alpha''$  phase  
5 will not be changed in order to keep a coherent notation in the whole paper. Actually, they  
6 correspond to the sense of twinning of  $\beta$  phase.  
7  
8  
9  
10  
11  
12  
13  
14  
15  
16  
17  
18  
19  
20  
21  
22  
23  
24  
25  
26  
27  
28  
29  
30  
31  
32  
33  
34  
35  
36  
37  
38  
39  
40  
41  
42  
43  
44  
45  
46  
47  
48  
49  
50  
51  
52  
53  
54  
55  
56  
57  
58  
59  
60  
61  
62  
63  
64  
65

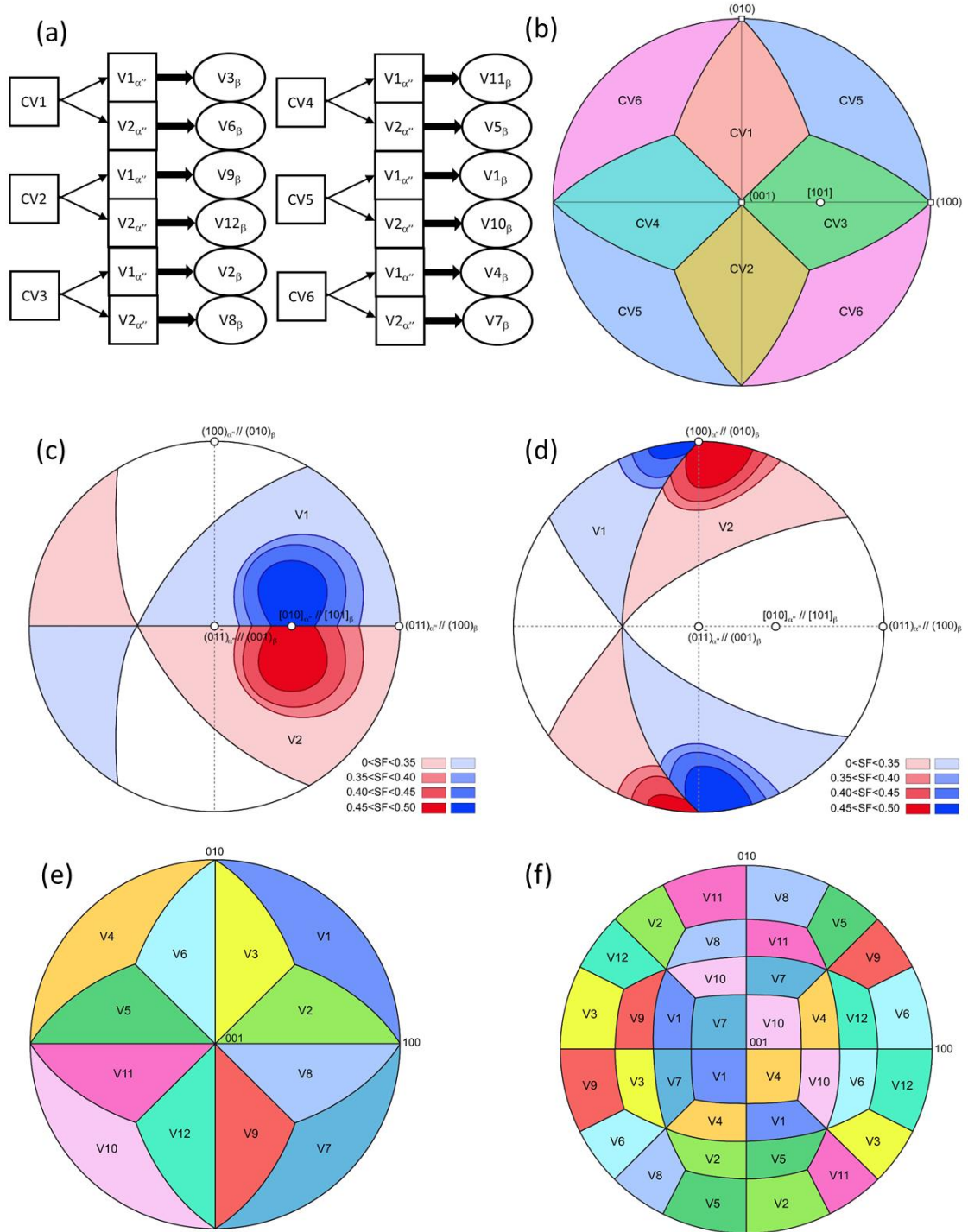


Fig. 7 Correspondences between variants of martensite, twin variants in martensite and twin variants in  $\beta$  phase (a); IPF showing variant selection of  $\alpha''$  martensite as a function of TD (b); IPFs of positive Schmid factor values of  $\{110\}\langle\bar{1}10\rangle_{\alpha''}^{at}$  (c) and  $\{110\}\langle\bar{1}\bar{1}0\rangle_{\alpha''}^t$  (d) in CV3 of  $\alpha''$  martensite; IPFs of maximum Schmid factor values of  $\{112\}\langle\bar{1}1\bar{1}\rangle_{\beta}^{at}$  and  $\{112\}\langle\bar{1}\bar{1}1\rangle_{\beta}^t$  twinning systems.

### 3.5. Twinning system activation in alloys exhibiting SIM transformation

1 Results of previous sections focused on a specific observation in a given single crystal. Let us  
 2 now generalize these results to any crystallographic orientation. Observed twins in  $\beta$  phase  
 3  
 4 are presently the result of a twinning operation in  $\alpha''$  martensite and a reverse SIM  
 5  
 6 transformation of  $\alpha''$  martensite twins. The formation of each  $\beta$  twin variant actually  
 7  
 8 corresponds to a process composed of two successive variant selections. The first step is the  
 9  
 10 selection between the 6 CVs during SIM transformation and the second step is the selection  
 11  
 12 between the two  $\{110\}\langle 110 \rangle_{\alpha''}$  twin variants. As only 2 twin variants exist for  $\{110\}\langle 110 \rangle_{\alpha''}$   
 13  
 14 twinning in  $\alpha''$ , only 2 of the 12  $\{112\}\langle 111 \rangle_{\beta}$  possible twin variants can be observed in  $\beta$   
 15  
 16 phase for a given CV. In the case of the present single crystal, CV3 is activated by tensile  
 17  
 18 stress. The application of CV3 BOR shows that only  $V_{2\beta}$  and  $V_{8\beta}$  fit with  $V_{1\alpha''}$  and  $V_{2\alpha''}$   
 19  
 20 respectively. However, the six possible CVs offered by SIM transformation combined with  
 21  
 22 the two possible variants of twinning in  $\alpha''$  phase cover the twelve variants of twinning in  $\beta$   
 23  
 24 phase. Fig 7a summarizes then these correspondences. Note that this process can operate with  
 25  
 26  $\{112\}\langle 11\bar{1} \rangle_{\beta}^{at}$  and  $\{110\}\langle \bar{1}10 \rangle_{\alpha''}^{at}$ , or with  $\{112\}\langle \bar{1}\bar{1}1 \rangle_{\beta}^t$  and  $\{110\}\langle 1\bar{1}0 \rangle_{\alpha''}^t$ . This first step  
 27  
 28 can be drawn as an inverse pole figure (IPF) showing the domains of selected CVs as a  
 29  
 30 function of the orientation of the tensile axis TD (Fig. 7b). The selected CV is then the one  
 31  
 32 leading to the maximum strain along the tensile axis among the 6 CVs as described in section  
 33  
 34 2.2. Considering the present single crystal, it can be seen on this figure that a  $[101]_{\beta}$   
 35  
 36 orientation of TD leads actually to CV3 under tensile stress.  
 37  
 38  
 39  
 40  
 41  
 42  
 43  
 44  
 45  
 46  
 47  
 48  
 49  
 50  
 51  
 52  
 53  
 54  
 55  
 56  
 57  
 58  
 59  
 60  
 61  
 62  
 63  
 64  
 65

1 positive  $m$  values of  $\{110\}\bar{1}10\}_{\alpha''}^{at}$  (Fig. 7c) coincide with the CV3 domain of Fig. 7b  
 2  
 3 whereas it is not the case for  $\{110\}1\bar{1}0\}_{\alpha''}^t$  (Fig. 7d). Therefore, only  $\{110\}\bar{1}10\}_{\alpha''}^{at}$  can  
 4  
 5 accommodate a tensile strain when CV3 is selected as in the present single crystal. This result  
 6  
 7 can be now generalized to any variant as detailed hereafter.  
 8  
 9

10 The same procedure can be done directly into the  $\beta$  phase for the variant selection of both  
 11  
 12 twinning and antitwinning  $\{112\}111\}_{\beta}$  modes. IPFs of maximal positive  $m$  values as a  
 13  
 14 function of the tensile direction of  $\{112\}11\bar{1}\}_{\beta}^{at}$  and  $\{112\}\bar{1}\bar{1}1\}_{\beta}^t$  systems are represented in  
 15  
 16 Fig. 7e and Fig 7f, respectively. The criterion of selection is then the maximum positive  $m$   
 17  
 18 value belong the 12 twin variants. The superimposition of Fig. 7b and Fig. 7e shows a perfect  
 19  
 20 fitting between the domains of activated CVs (Fig. 7b) and activated twin variants of  
 21  
 22  $\{112\}11\bar{1}\}_{\beta}^{at}$  (Fig. 7e). In other words, the CV selection of  $\alpha''$  martensite followed by the  
 23  
 24 twin variant selection in the activated  $\alpha''$  CV leads to the same result than considering directly  
 25  
 26 the variant selection of  $\{112\}11\bar{1}\}_{\beta}^{at}$  antitwins in  $\beta$  phase. The CV selection of  $\alpha''$  martensite  
 27  
 28 for a tensile test always gives a crystal of martensite favorably orientated to produce  
 29  
 30  $\{112\}11\bar{1}\}_{\beta}^{at}$  twins after reverse SIM transformation. Conversely, the Fig. 7f shows the  
 31  
 32 variant selection of classical  $\{112\}\bar{1}\bar{1}1\}_{\beta}^t$  twins in  $\beta$  phase, i.e. the domain of preferential  
 33  
 34 activation of each twin variant if no SIM is considered. Taking again the present single crystal  
 35  
 36 with the tensile direction of [101] as an example,  $\{112\}\bar{1}\bar{1}1\}_{\beta}^t$  twin variants  $V_{4\beta}$ ,  $V_{6\beta}$ ,  $V_{10\beta}$   
 37  
 38 or  $V_{12\beta}$  would be expected to be activated (Fig. 7f). However, the superimposition of Fig. 7f  
 39  
 40 with Fig. 7b shows that the CV3 of  $\alpha''$  martensite is activated, and, regarding the possible  
 41  
 42 twin variants of  $\{112\}\bar{1}\bar{1}1\}_{\beta}^t$  possibly formed from the reversion of twins in  $\alpha''$  (Fig. 7a),  
 43  
 44 only  $V_{2\beta}$  and  $V_{8\beta}$  can be produced. Finally, this point highlights that the classical  
 45  
 46  $\{112\}\bar{1}\bar{1}1\}_{\beta}^t$  twinning system can never be formed in  $\beta$  phase due to the CV selection of  
 47  
 48 martensite occurring during a tensile test, whatever the tensile direction. While this CV  
 49  
 50  
 51  
 52  
 53  
 54  
 55  
 56  
 57  
 58  
 59  
 60  
 61  
 62  
 63  
 64  
 65

1 selection promotes the formation of non-classical  $\{112\}\langle 11\bar{1}\rangle_{\beta}^{at}$  twins in the antitwinning  
2 sense through the activation and the reversion of  $\{110\}\langle \bar{1}10\rangle_{\alpha''}^{at}$  twins in  $\alpha''$  martensite.  
3  
4 Therefore, a careful examination of activated  $\{112\}\langle 111\rangle_{\beta}$  twin variants by Schmid factor  
5 analysis allows to determine if a SIM transformation has occurred: If the observed  
6  
7  $\{112\}\langle 111\rangle_{\beta}$  twins are in the twinning sense of classical bcc structures, twins are directly  
8  
9 formed into the  $\beta$  phase, while  $\{112\}\langle 111\rangle_{\beta}$  twins in the antitwinning sense are the proof of  
10  
11 the reversion of twins previously formed into a SIM  $\alpha''$  phase.  
12  
13  
14  
15  
16  
17  
18  
19  
20

#### 21 4. Conclusions

22  
23 A single crystal of metastable  $\beta$  Ti-24Nb-4Zr-8Sn alloy was studied. *In situ* SXRD during  
24  
25 cyclic tensile test shows that full martensitic transformation is achieved when plastic  
26  
27 deformation begins. Deformation twins are observed *post mortem* after tensile test and are  
28  
29 identified as  $\{112\}\langle 111\rangle_{\beta}$  twins. Careful Schmid factor analysis of the observed  
30  
31  $\{112\}\langle 111\rangle_{\beta}$  twins shows that they are  $\{112\}\langle 11\bar{1}\rangle_{\beta}^{at}$  antitwins with a twinning direction  
32  
33 opposite to that of classical  $\{112\}\langle \bar{1}\bar{1}1\rangle_{\beta}^t$  twins of bcc structure, i.e. along the antitwinning  
34  
35 direction.  
36  
37  
38  
39

40  
41 This unusual observation is explained by the stress-induced martensitic transformation  
42  
43 occurring during tensile test. Observed twins in  $\beta$  phase are actually the result of the reversion  
44  
45 during the reverse SIM transformation of activated  $\{110\}\langle \bar{1}10\rangle_{\alpha''}^{at}$  twins in  $\alpha''$  martensite. The  
46  
47 magnitude of shuffle drops then from  $1/2 [1\bar{1}1]_{\beta}$  if these twins were directly formed in  $\beta$   
48  
49 phase, to  $1/5 [\bar{1}10]_{\alpha''}$  after SIM transformation, making it easier to activate in  $\alpha''$  phase.  
50  
51  
52 Moreover, variant selection of stress-induced martensite always leads to a martensitic crystal  
53  
54 which is favorably oriented for  $\{110\}\langle \bar{1}10\rangle_{\alpha''}^{at}$  and unfavorably oriented for  $\{110\}\langle 1\bar{1}0\rangle_{\alpha''}^t$   
55  
56 twinning system, according to Schmid factor analysis. Finally, this former feature  
57  
58  
59  
60  
61  
62  
63  
64  
65

1 demonstrates that the occurrence of  $\alpha''$  SIM transformation promotes the observation of  
2  $\{112\}\{11\bar{1}\}_\beta^{at}$  antitwins and totally impedes the formation of classical  $\{112\}\{\bar{1}\bar{1}1\}_\beta^t$  twins of  
3  
4 bcc structures due to a combination of variant selection of stress-induced martensite and  
5  
6 occurrence of reverse martensitic transformation.  
7  
8  
9

## 10 11 12 **Acknowledgements**

13  
14 The authors acknowledge the European Synchrotron Radiation Facility for provision of  
15 synchrotron radiation facilities and would like to thank Yves Watier for assistance in using  
16 the beamline ID31 (presently ID22). The authors also acknowledge the THEMIS platform of  
17 the University of Rennes for providing access to TEM facilities. The authors finally  
18 acknowledge Prof. Yulin Hao and Dr. Haoliang Wang in Institute of Metal Research Chinese  
19 Academy of Sciences for providing single crystal.  
20  
21  
22  
23  
24

25 This work was financially supported by the National Science Foundation for Young  
26 Scientists of China (Grant No. 51801199).  
27  
28  
29  
30

## 31 32 **Compliance with Ethical Standards:**

33  
34 The authors declare that they have no conflict of interest.  
35  
36  
37  
38  
39  
40

## 41 42 **References**

- 43 [1] Niinomi M (2003) Fatigue performance and cyto-toxicity of low rigidity titanium alloy,  
44 Ti–29Nb–13Ta–4.6Zr. *Biomater* 24:2673-2683. doi:10.1016/S0142-9612(03)00069-3  
45 [2] Geetha M, Singh AK, Asokamani R, Gogia AK (2009) Ti based biomaterials, the ultimate  
46 choice for orthopaedic implants - A review. *Prog Mater Sci* 54:397-425.  
47 doi:10.1016/j.pmatsci.2008.06.004  
48 [3] Cimpean A, Mitran V, Ciofrangeanu CM, Galateanu B, Bertrand E, Gordin D-M,  
49 Iordachescu D, Gloriant T (2012) Osteoblast cell behavior on the new beta-type Ti–25Ta–  
50 25Nb alloy. *Mater Sci Eng C* 32:1554-1563. doi:10.1016/j.msec.2012.04.042  
51 [4] Castany P, Gordin DM, Drob SI, Vasilescu C, Mitran V, Cimpean A, Gloriant T (2016)  
52 Deformation mechanisms and biocompatibility of the superelastic Ti–23Nb–0.7Ta–2Zr–0.5N  
53 alloy. *Shape Mem Superel* 2:18-28. doi:10.1007/s40830-016-0057-0  
54 [5] Gordin DM, Ion R, Vasilescu C, Drob SI, Cimpean A, Gloriant T (2014) Potentiality of  
55 the “Gum Metal” titanium-based alloy for biomedical applications. *Mater Sci Eng C* 44:362-  
56 370. doi:10.1016/j.msec.2014.08.003  
57  
58  
59  
60  
61  
62  
63  
64  
65

- [6] Bertrand E, Gloriant T, Gordin DM, Vasilescu E, Drob P, Vasilescu C, Drob SI (2010) Synthesis and characterisation of a new superelastic Ti-25Ta-25Nb biomedical alloy. *J Mech Behav Biomed Mater* 3:559-564. doi:10.1016/j.jmbbm.2010.06.007
- [7] Laheurte P, Prima F, Eberhardt A, Gloriant T, Wary M, Patoor E (2010) Mechanical properties of low modulus  $\beta$  titanium alloys designed from the electronic approach. *J Mech Behav Biomed Mater* 3:565-573. doi:10.1016/j.jmbbm.2010.07.001
- [8] Bertrand E, Castany P, Gloriant T (2013) Investigation of the martensitic transformation and the damping behavior of a superelastic Ti-Ta-Nb alloy. *Acta Mater* 61:511-518. doi:10.1016/j.actamat.2012.09.065
- [9] Hao YL, Li SJ, Sun SY, Yang R (2006) Effect of Zr and Sn on Young's modulus and superelasticity of Ti-Nb-based alloys. *Mater Sci Eng A* 441:112-118. doi:10.1016/j.msea.2006.09.051
- [10] Fernandes Santos P, Niinomi M, Liu H, Cho K, Nakai M, Trenggono A, Champagne S, Hermawan H, Narushima T (2016) Improvement of microstructure, mechanical and corrosion properties of biomedical Ti-Mn alloys by Mo addition. *Mater Design* 110:414-424. doi:10.1016/j.matdes.2016.07.115
- [11] Zhao X, Niinomi M, Nakai M, Miyamoto G, Furuhashi T (2011) Microstructures and mechanical properties of metastable Ti-30Zr-(Cr, Mo) alloys with changeable Young's modulus for spinal fixation applications. *Acta Biomater* 7:3230-3236. doi:10.1016/j.actbio.2011.04.019
- [12] Castany P, Ramarolahy A, Prima F, Laheurte P, Curfs C, Gloriant T (2015) In situ synchrotron X-ray diffraction study of the martensitic transformation in superelastic Ti-24Nb-0.5N and Ti-24Nb-0.5O alloys. *Acta Mater* 88:102-111. doi:10.1016/j.actamat.2015.01.014
- [13] Gao JJ, Thibon I, Laillé D, Castany P, Gloriant T (2019) Influence of texture and transformation strain on the superelastic performance of a new Ti-20Zr-3Mo-3Sn alloy. *Mater Sci Eng A* 762:138075. doi:10.1016/j.msea.2019.138075
- [14] Obbard EG, Hao YL, Akahori T, Talling RJ, Niinomi M, Dye D, Yang R (2010) Mechanics of superelasticity in Ti-30Nb-(8-10)Ta-5Zr alloy. *Acta Mater* 58:3557-3567. doi:10.1016/j.actamat.2010.02.010
- [15] Tahara M, Kim HY, Hosoda H, Miyazaki S (2009) Cyclic deformation behavior of a Ti-26 at.% Nb alloy. *Acta Mater* 57:2461-2469. doi:10.1016/j.actamat.2009.01.037
- [16] Ijaz MF, Kim HY, Hosoda H, Miyazaki S (2014) Effect of Sn addition on stress hysteresis and superelastic properties of a Ti-15Nb-3Mo alloy. *Scripta Mater* 72-73:29-32. doi:10.1016/j.scriptamat.2013.10.007
- [17] Bertrand E, Castany P, Péron I, Gloriant T (2011) Twinning system selection in a metastable  $\beta$ -titanium alloy by Schmid factor analysis. *Scripta Mater* 64:1110-1113. doi:10.1016/j.scriptamat.2011.02.033
- [18] Ramarolahy A, Castany P, Prima F, Laheurte P, Péron I, Gloriant T (2012) Microstructure and mechanical behavior of superelastic Ti-24Nb-0.5O and Ti-24Nb-0.5N biomedical alloys. *J Mech Behav Biomed Mater* 9:83-90. doi:10.1016/j.jmbbm.2012.01.017
- [19] Lin F, Marteleur M, Jacques PJ, Delannay L (2018) Transmission of {332}  $\langle$ 113 $\rangle$  twins across grain boundaries in a metastable  $\beta$ -titanium alloy. *Int J Plast* 105:195-210. doi:10.1016/j.ijplas.2018.02.012
- [20] Cho K, Morioka R, Harjo S, Kawasaki T, Yasuda HY (2020) Study on formation mechanism of {332} $\langle$ 113 $\rangle$  deformation twinning in metastable  $\beta$ -type Ti alloy focusing on stress-induced  $\alpha''$  martensite phase. *Scripta Mater* 177:106-111. doi:10.1016/j.scriptamat.2019.10.011
- [21] Min X, Chen X, Emura S, Tsuchiya K (2013) Mechanism of twinning-induced plasticity in  $\beta$ -type Ti-15Mo alloy. *Scripta Mater* 69:393-396. doi:10.1016/j.scriptamat.2013.05.027

- 1 [22] Yang Y, Castany P, Hao YL, Gloriant T (2020) Plastic deformation via hierarchical  
2 nano-sized martensitic twinning in the metastable  $\beta$  Ti-24Nb-4Zr-8Sn alloy. *Acta Mater*  
3 194:27-39. doi:10.1016/j.actamat.2020.04.021
- 4 [23] Castany P, Besse M, Gloriant T (2012) In situ TEM study of dislocation slip in a  
5 metastable  $\beta$  titanium alloy. *Scripta Mater* 66:371-373. doi:10.1016/j.scriptamat.2011.11.036
- 6 [24] Momprou F, Tingaud D, Chang Y, Gault B, Dirras G (2018) Conventional vs harmonic-  
7 structured  $\beta$ -Ti-25Nb-25Zr alloys: A comparative study of deformation mechanisms. *Acta*  
8 *Mater* 161:420-430. doi:10.1016/j.actamat.2018.09.032
- 9 [25] Castany P, Besse M, Gloriant T (2011) Dislocation mobility in gum metal beta-titanium  
10 alloy studied via in situ transmission electron microscopy. *Phys Rev B* 84:020201.  
11 doi:10.1103/PhysRevB.84.020201
- 12 [26] Besse M, Castany P, Gloriant T (2011) Mechanisms of deformation in gum metal TNTZ-  
13 O and TNTZ titanium alloys: A comparative study on the oxygen influence. *Acta Mater*  
14 59:5982-5988. doi:10.1016/j.actamat.2011.06.006
- 15 [27] Bertrand E, Castany P, Yang Y, Menou E, Gloriant T (2016) Deformation twinning in  
16 the full- $\alpha$ " martensitic Ti-25Ta-20Nb shape memory alloy. *Acta Mater* 105:94-103.  
17 doi:10.1016/j.actamat.2015.12.001
- 18 [28] Kim HY, Ikehara Y, Kim JI, Hosoda H, Miyazaki S (2006) Martensitic transformation,  
19 shape memory effect and superelasticity of Ti-Nb binary alloys. *Acta Mater* 54:2419-2429.  
20 doi:10.1016/j.actamat.2006.01.019
- 21 [29] Tahara M, Kim HY, Hosoda H, Nam T-H, Miyazaki S (2010) Effect of nitrogen addition  
22 and annealing temperature on superelastic properties of Ti-Nb-Zr-Ta alloys. *Mater Sci Eng*  
23 *A* 527:6844-6852. doi:10.1016/j.msea.2010.07.052
- 24 [30] Kim HY, Sasaki T, Okutsu K, Kim JI, Inamura T, Hosoda H, Miyazaki S (2006) Texture  
25 and shape memory behavior of Ti-22Nb-6Ta alloy. *Acta Mater* 54:423-433.  
26 doi:10.1016/j.actamat.2005.09.014
- 27 [31] Bignon M, Bertrand E, Tancret F, Rivera-Díaz-del-Castillo PEJ (2019) Modelling  
28 martensitic transformation in titanium alloys: The influence of temperature and deformation.  
29 *Materialia* 7:100382. doi:10.1016/j.mtla.2019.100382
- 30 [32] Brozek C, Sun F, Vermaut P, Millet Y, Lenain A, Embury D, Jacques PJ, Prima F (2016)  
31 A  $\beta$ -titanium alloy with extra high strain-hardening rate: Design and mechanical properties.  
32 *Scripta Mater* 114:60-64. doi:10.1016/j.scriptamat.2015.11.020
- 33 [33] Danard Y, Poulain R, Garcia M, Guillou R, Thiaudière D, Mantri S, Banerjee R, Sun F,  
34 Prima F (2019) Microstructure design and in-situ investigation of TRIP/TWIP effects in a  
35 forged dual-phase Ti-10V-2Fe-3Al alloy. *Materialia* 8:100507.  
36 doi:10.1016/j.mtla.2019.100507
- 37 [34] Lilensten L, Danard Y, Brozek C, Mantri S, Castany P, Gloriant T, Vermaut P, Sun F,  
38 Banerjee R, Prima F (2019) On the heterogeneous nature of deformation in a strain-  
39 transformable beta metastable Ti-V-Cr-Al alloy. *Acta Mater* 162:268-276.  
40 doi:10.1016/j.actamat.2018.10.003
- 41 [35] Sun F, Zhang JY, Marteleur M, Brozek C, Rauch EF, Veron M, Vermaut P, Jacques PJ,  
42 Prima F (2015) A new titanium alloy with a combination of high strength, high strain  
43 hardening and improved ductility. *Scripta Mater* 94:17-20.  
44 doi:10.1016/j.scriptamat.2014.09.005
- 45 [36] Laplanche G, Pfetzinger-Micklich J, Eggeler G (2014) Sudden stress-induced  
46 transformation events during nanoindentation of NiTi shape memory alloys. *Acta Materialia*  
47 78:144-160. doi:10.1016/j.actamat.2014.05.061
- 48 [37] Otsuka K, Ren X (2005) Physical metallurgy of Ti-Ni-based shape memory alloys. *Prog*  
49 *Mater Sci* 50:511-678. doi:10.1016/j.pmatsci.2004.10.001
- 50  
51  
52  
53  
54  
55  
56  
57  
58  
59  
60  
61  
62  
63  
64  
65

- 1 [38] Gall K, Sehitoglu H (1999) The role of texture in tension–compression asymmetry in  
2 polycrystalline NiTi. *Int J Plast* 15:69-92. doi:10.1016/S0749-6419(98)00060-6
- 3 [39] Gao X, Huang M, Brinson LC (2000) A multivariant micromechanical model for SMAs  
4 Part 1. Crystallographic issues for single crystal model. *Int J Plast* 16:1345-1369.  
5 doi:10.1016/S0749-6419(00)00013-9
- 6 [40] Castany P, Gloriant T, Sun F, Prima F (2018) Design of strain-transformable titanium  
7 alloys. *C R Phys* 19:710-720. doi:10.1016/j.crhy.2018.10.004
- 8 [41] Ijaz MF, Kim HY, Hosoda H, Miyazaki S (2015) Superelastic properties of biomedical  
9 (Ti-Zr)-Mo-Sn alloys. *Mater Sci Eng C* 48:11-20. doi:10.1016/j.msec.2014.11.010
- 10 [42] Kim HY, Hashimoto S, Kim JI, Inamura T, Hosoda H, Miyazaki S (2006) Effect of Ta  
11 addition on shape memory behavior of Ti–22Nb alloy. *Mater Sci Eng A* 417:120-128.  
12 doi:10.1016/j.msea.2005.10.065
- 13 [43] Kim JI, Kim HY, Inamura T, Hosoda H, Miyazaki S (2005) Shape memory  
14 characteristics of Ti–22Nb–(2–8)Zr(at.%) biomedical alloys. *Mater Sci Eng A* 403:334-339.  
15 doi:10.1016/j.msea.2005.05.050
- 16 [44] Ijaz MF, Héraud L, Castany P, Thibon I, Gloriant T (2020) Superelastic Behavior of  
17 Biomedical Metallic Alloys. *Metall Mater Trans A* 51:3733-3741. doi:10.1007/s11661-020-  
18 05840-y
- 19 [45] Tahara M, Kim HY, Inamura T, Hosoda H, Miyazaki S (2011) Lattice modulation and  
20 superelasticity in oxygen-added  $\beta$ -Ti alloys. *Acta Mater* 59:6208-6218.  
21 doi:10.1016/j.actamat.2011.06.015
- 22 [46] Christian JW, Mahajan S (1995) Deformation twinning. *Prog Mater Sci* 39:1-157
- 23 [47] Tobe H, Kim HY, Inamura T, Hosoda H, Miyazaki S (2014) Origin of {332} twinning in  
24 metastable  $\beta$ -Ti alloys. *Acta Mater* 64:345-355. doi:10.1016/j.actamat.2013.10.048
- 25 [48] Qian B, Zhang J, Fu Y, Sun F, Wu Y, Cheng J, Vermaut P, Prima F (2021) In-situ  
26 microstructural investigations of the TRIP-to-TWIP evolution in Ti-Mo-Zr alloys as a  
27 function of Zr concentration. *J Mater Sci Tech* 65:228-237. doi:10.1016/j.jmst.2020.04.078
- 28 [49] Castany P, Yang Y, Bertrand E, Gloriant T (2016) Reversion of a parent {130}<310> $\alpha$ "  
29 martensitic twinning system at the origin of {332}<113> $\beta$  twins observed in metastable beta  
30 titanium alloys. *Phys Rev Lett* 117:245501. doi:10.1103/PhysRevLett.117.245501
- 31 [50] Lai MJ, Tasan CC, Raabe D (2016) On the mechanism of {332} twinning in metastable  $\beta$   
32 titanium alloys. *Acta Mater* 111:173-186. doi:10.1016/j.actamat.2016.03.040
- 33 [51] Chen B, Sun W (2018) Transitional structure of {332}<113>  $\beta$  twin boundary in a  
34 deformed metastable  $\beta$ -type Ti-Nb-based alloy, revealed by atomic resolution electron  
35 microscopy. *Scripta Mater* 150:115-119. doi:10.1016/j.scriptamat.2018.03.009
- 36 [52] Chai YW, Kim HY, Hosoda H, Miyazaki S (2009) Self-accommodation in Ti-Nb shape  
37 memory alloys. *Acta Mater* 57:4054-4064. doi:10.1016/j.actamat.2009.04.051
- 38 [53] Inamura T, Kim JI, Kim HY, Hosoda H, Wakashima K, Miyazaki S (2007) Composition  
39 dependent crystallography of  $\alpha$ "-martensite in Ti-Nb-based  $\beta$ -titanium alloy. *Philos Mag*  
40 87:3325-3350. doi: 10.1080/14786430601003874
- 41 [54] Tahara M, Okano N, Inamura T, Hosoda H (2017) Plastic deformation behaviour of  
42 single-crystalline martensite of Ti-Nb shape memory alloy. *Sci Rep* 7:15715.  
43 doi:10.1038/s41598-017-15877-6
- 44 [55] Ping DH, Yamabe-Mitarai Y, Cui CY, Yin FX, Choudhry MA (2008) Stress-induced  $\alpha$ "  
45 martensitic (110) twinning in  $\beta$ -Ti alloys. *Appl Phys Lett* 93:151911. doi:10.1063/1.3002295
- 46 [56] Yang Y, Castany P, Bertrand E, Cornen M, Lin JX, Gloriant T (2018) Stress release-  
47 induced interfacial twin boundary  $\omega$  phase formation in a  $\beta$  type Ti-based single crystal  
48 displaying stress-induced  $\alpha$ " martensitic transformation. *Acta Mater* 149:97-107.  
49 doi:10.1016/j.actamat.2018.02.036
- 50  
51  
52  
53  
54  
55  
56  
57  
58  
59  
60  
61  
62  
63  
64  
65

1 [57] Jabir H, Fillon A, Castany P, Gloriant T (2019) Crystallographic orientation dependence  
2 of mechanical properties in the superelastic Ti-24Nb-4Zr-8Sn alloy. *Phys Rev Mater*  
3 3:063608. doi:10.1103/PhysRevMaterials.3.063608

4 [58] Inamura T, Yamamoto Y, Hosoda H, Kim HY, Miyazaki S (2010) Crystallographic  
5 orientation and stress-amplitude dependence of damping in the martensite phase in textured  
6 Ti-Nb-Al shape memory alloy. *Acta Mater* 58:2535-2544. doi:10.1016/j.actamat.2009.12.040  
7  
8  
9  
10  
11  
12  
13  
14  
15  
16  
17  
18  
19  
20  
21  
22  
23  
24  
25  
26  
27  
28  
29  
30  
31  
32  
33  
34  
35  
36  
37  
38  
39  
40  
41  
42  
43  
44  
45  
46  
47  
48  
49  
50  
51  
52  
53  
54  
55  
56  
57  
58  
59  
60  
61  
62  
63  
64  
65

